



# Theoretical Study on $^{10}\text{C}$ Elastic Scattering Cross Sections Using Different Cluster Density Distributions and Different Potentials

Sunday D. Olorunfunmi<sup>a,\*</sup>, A. Bahini<sup>b</sup>, Adenike S. Olatinwo<sup>a</sup>

<sup>a</sup>Department of Physics & Engineering Physics, Obafemi Awolowo University, Ile-Ife 220005, Osun State, Nigeria

<sup>b</sup>Themba Laboratory for Accelerator Based Sciences, Somerset West 7129, South Africa

## Abstract

Elastic scattering cross sections are a fundamental aspect of nuclear physics research, and studying the cross sections of various nuclei can provide important insights into the behavior of nuclei. In this study, the elastic scattering cross sections of  $^{10}\text{C}$  projectile by  $^{27}\text{Al}$ ,  $^{58}\text{Ni}$ , and  $^{208}\text{Pb}$  target nuclei are analyzed. The aim of this study is to investigate the cluster structure of  $^{10}\text{C}$  and the sensitivity of the elastic scattering cross sections to different potentials. To achieve this objective, the double folding optical model and a simple cluster approach are used to analyze the cross sections. The real part of the optical potential is obtained by folding two different effective interactions, Michigan-3-Yukawa (M3Y) and Jeukenne-Lejeune-Mahaux (JLM), with four different cluster density distributions of the  $^{10}\text{C}$  nucleus:  $^6\text{Be} + \alpha$ ,  $^9\text{B} + p$ ,  $^8\text{Be} + p + p$ , and  $\alpha + \alpha + p + p$ . The imaginary part is taken to be a Woods-Saxon phenomenological form. The sensitivity of the elastic scattering cross sections to different potentials is assessed by comparing the results obtained using different potentials. The cluster structure of  $^{10}\text{C}$  is validated by comparing the theoretical results with experimental data. The results show that the cross sections are sensitive to the choice of potential used and that the cluster structure of  $^{10}\text{C}$  is validated. The theoretical results show reasonable agreement with the experimental data.

DOI:10.46481/jnsps.2023.1392

**Keywords:** Elastic scattering, density distribution, Optical model, cluster model.

## Article History :

Received: 11 February 2023

Received in revised form: 25 April 2023

Accepted for publication: 10 May 2023

Published: 21 May 2023

© 2023 The Author(s). Published by the Nigerian Society of Physical Sciences under the terms of the Creative Commons Attribution 4.0 International license (<https://creativecommons.org/licenses/by/4.0>). Further distribution of this work must maintain attribution to the author(s) and the published article's title, journal citation, and DOI.

Communicated by: O. J. Oluwadare

## 1. Introduction

There has been significant interest in studying reaction mechanisms involving weakly bound neutron- and proton-rich nuclei, especially because of their astrophysical importance or applications [1, 2, 3, 4, 5, 6]. One of such weakly bound nuclei that is of interest is the unstable proton-rich  $^{10}\text{C}$ , which exhibits a three-cluster structure and can decay into  $^6\text{Be} + \alpha$ ,  $^9\text{B} + p$ , and

$^8\text{Be} + p + p$  channels with binding energies of 3.821, 4.006, and 5.101 MeV, respectively [7, 8]. Curtis *et al.*, [9] studied the break up reaction of  $^{10}\text{C}$  and concluded that the proton-rich nucleus can also decay by  $\alpha + \alpha + p + p$  channel.

The elastic scattering angular distributions of  $^{10}\text{C} + ^{27}\text{Al}$  at incident energy of 29.1 MeV have been measured and theoretically analyzed using optical model potential constructed from the combination of real São Paulo potential (SPP), imaginary Woods-Saxon potential and complex polarization potentials [10]. The study concluded that the inclusion of the volume and surface complex polarized potentials is needed in order to

\*Corresponding author tel. no: +2349042713841

Email address: [sundayolorunfunmi@gmail.com](mailto:sundayolorunfunmi@gmail.com) (Sunday D. Olorunfunmi)

successfully describe the data. These polarized potentials account for fusion and direct coupling. These distributions were recently analyzed by Aygun [11] using double folding optical potential with the real potential constructed by folding M3Y effective interaction with relativistic mean-field density distribution of  $^{10}\text{C}$  and Woods-Saxon (WS) imaginary potential. A new set of global potential was obtained for the carbon isotope.

Yang *et al.*, [7] measured the quasi-elastic scattering angular distributions of  $^{10}\text{C} + ^{208}\text{Pb}$  at 226 and 256 MeV. Very recently, the elastic scattering cross sections of the same reaction at 66 MeV was measured by Linares *et al.*, [8]. The data were analyzed and compared with the results of optical model calculations performed using the SPP nucleus-nucleus interaction. Again, the same data at 256 MeV was further analyzed in Ref. [11] using optical-model based double folding potentials.

Recently, Guimaraes *et al.*, [12] measured the elastic scattering of  $^{10}\text{C}$  on  $^{58}\text{Ni}$  target nuclei at incident energy of 35.3 MeV with the purpose of studying the coupling effect in the reaction. They analyzed the measured data using microscopic approach within the framework of coupled-channels (CC) and coupled-reaction channels (CRC) models. Results of the two models could not describe the data satisfactorily. In order to improve the description of the data they performed continuum-discretized coupled-channels (CDCC) calculations. In CDCC calculations the  $^{10}\text{C}$  nucleus was assumed to decay by two channels:  $^9\text{B} + p$  and  $^6\text{Be} + \alpha$ . In the end they were able to achieve a fair agreement between the theoretical calculations and experimental data, but the need for a more realistic theoretical calculations was emphasized. Consequent upon this, Aygun [13] carried out a comprehensive theoretical analysis of this reaction using different potentials and simple cluster model. The study considered  $^6\text{Be} + \alpha$ ,  $^9\text{B} + p$ , and  $^8\text{Be} + p + p$  cluster configurations for  $^{10}\text{C}$ , and found that the  $^6\text{Be} + \alpha$  configuration describe the data better than  $^9\text{B} + p$ , and  $^8\text{Be} + p + p$  cases. It was recommended that the cluster structure of  $^{10}\text{C}$  be evaluated in the analysis of elastic scattering reactions of  $^{10}\text{C}$  with other target nuclei.

In this present study, the elastic scattering cross section of  $^{10}\text{C}$  projectile nucleus from  $^{27}\text{Al}$ ,  $^{58}\text{Ni}$  and  $^{208}\text{Pb}$  target nuclei are calculated using the complex optical model potential with folded real part and phenomenological Woods-Saxon imaginary part. The real part is constructed by folding two different effective nucleon-nucleon (NN) interactions M3Y and JLM with four different cluster density distributions of  $^{10}\text{C}$  nucleus. Here, we aim to study the structure effect in  $^{10}\text{C} + \text{Nucleus}$  reactions via different choice of simple cluster density distributions of  $^{10}\text{C}$  projectile nucleus and to investigate the sensitivity of  $^{10}\text{C} + \text{Nucleus}$  elastic scattering cross sections to different effective NN interactions.

## 2. Theoretical Formalism

### 2.1. The Optical model potential

The theoretical calculations were performed using the optical model of the form:

Table 1: The parameters of two-parameter Fermi (2pF) density distributions for the  $^{27}\text{Al}$ ,  $^{58}\text{Ni}$ , and  $^{208}\text{Pb}$  target nuclei.

Nucleus	$c$ (fm)	$z$ (fm)	$\rho_0$ (fm $^{-3}$ )	Reference
$^{27}\text{Al}$	2.840	0.569	0.2015	[14]
$^{58}\text{Ni}$	4.094	0.540	0.1720	[15]
$^{208}\text{Pb}$	6.620	0.551	0.1600	[14]

$$U(r) = V_{\text{Coul}}(r) - V(r) - iW(r), \quad (1)$$

where  $V_{\text{Coul}}(r)$  is the Coulomb potential,  $V(r)$  is the real potential and  $W(r)$  is the imaginary potential. The Coulomb potential is defined as:

$$V_{\text{Coul}}(r) = \begin{cases} \frac{1}{4\pi\epsilon_0} \frac{Z_p Z_T e^2}{r} & \text{if } r \geq R_{\text{Coul}} \\ \frac{1}{4\pi\epsilon_0} \frac{Z_p Z_T e^2}{2R_{\text{Coul}}} \left( 3 - \frac{r^2}{R_{\text{Coul}}^2} \right) & \text{if } r \leq R_{\text{Coul}} \end{cases} \quad (2)$$

with

$$R_{\text{Coul}} = 1.25(A_p^{(1/3)} + A_T^{(1/3)}), \quad (3)$$

where  $Z_{P(T)}$  and  $A_{P(T)}$  are the proton and mass number of the projectile (target) nuclei, respectively. In Refs. [16, 17], the Coulomb potential was used in a theoretical investigation of the half-life of certain nuclei. The real potential  $V(r)$  is obtained by using the double folding potential given as:

$$V(\vec{r}) = N_R \int d\vec{r}_1 \int d\vec{r}_2 \rho_P(\vec{r}) \rho_T(\vec{r}) v_{\text{NN}}(\vec{r}_{12}), \quad (4)$$

where  $\vec{r}_{12} = [\vec{r} - (\vec{r}_1 - \vec{r}_2)]$ ,  $N_R$  is the normalization constant,  $v_{\text{NN}}$  is the effective NN interaction, and  $\rho_P$  ( $\rho_T$ ) is the density distribution of the projectile (target). In this work, four different cluster density distributions of the projectile nucleus are considered, and each is introduced in the following section. The density distributions of target nuclei are obtained by using the two-parameter Fermi (2pF) density

$$\rho(r) = \frac{\rho_0}{1 + \exp\left(\frac{r-c}{z}\right)}, \quad (5)$$

where  $\rho_0$  is the maximum density (central density) of the nucleus and the Fermi-distribution parameters  $c$  and  $z$  describe the half-density radius and the diffuseness, respectively. Their numerical values are listed in Table 1. Two forms of effective NN interaction  $v_{\text{NN}}$  are considered, namely, M3Y and JLM. These two interactions are presented in the next section. The imaginary potential  $W(r)$  is taken in the Woods-Saxon form:

$$W(r) = \frac{W_0}{1 + \exp\left(\frac{r-r_1(A_p^{1/3} + A_T^{1/3})}{a_1}\right)}, \quad (6)$$

where  $W_0$ ,  $r_1$  and  $a_1$  represent the potential depth, the reduced radius, and the diffuseness parameter, respectively.

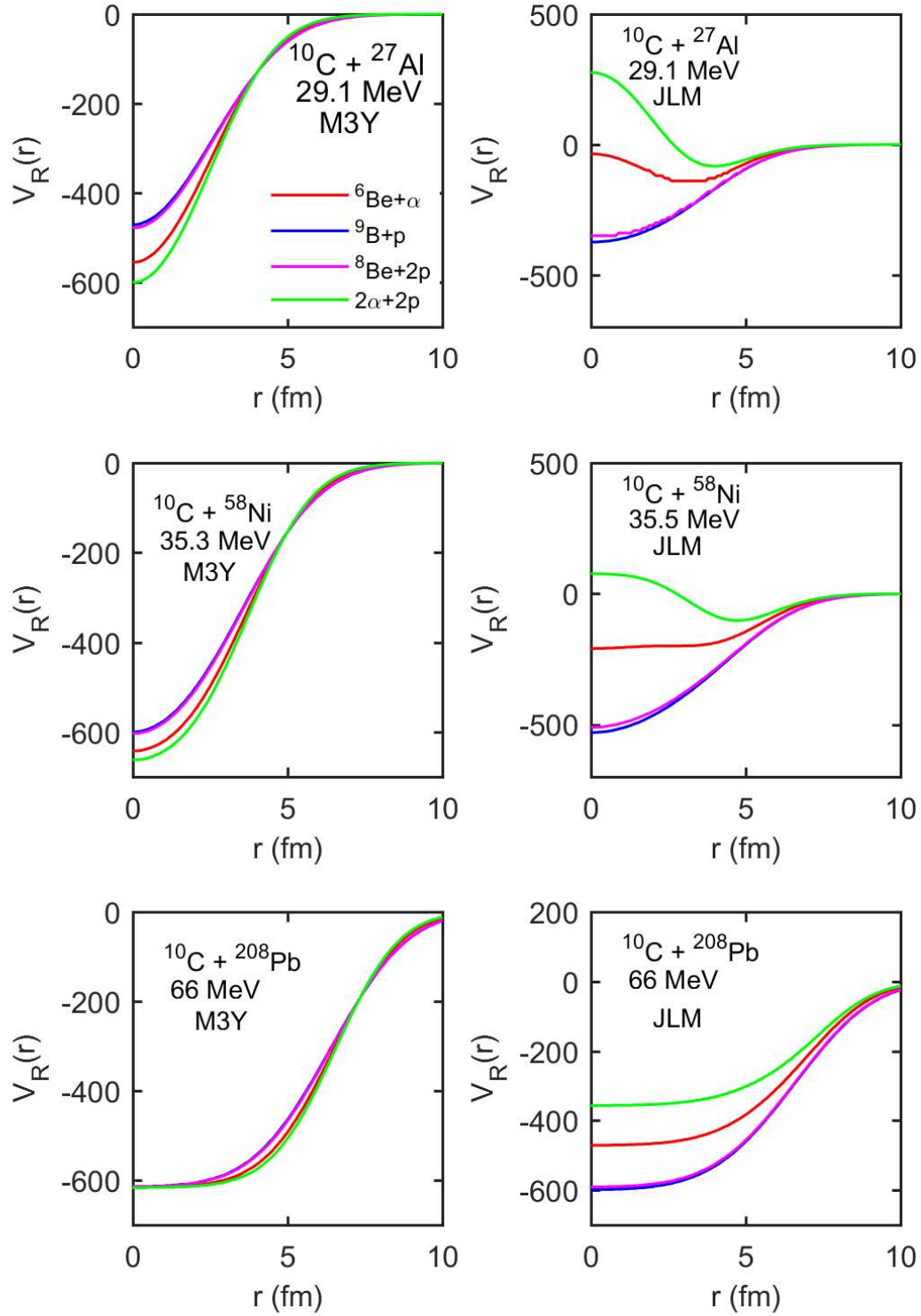


Figure 1: Real folded potential for  $^{10}\text{C} + ^{27}\text{Al}$  at 29.1 MeV,  $^{10}\text{C} + ^{58}\text{Ni}$  at 35.3 MeV and  $^{10}\text{C} + ^{208}\text{Pb}$  at 66 MeV, using M3Y and JLM effective interactions with  $^6\text{Be} + \alpha$ ,  $^9\text{B} + p$ ,  $^8\text{Be} + p + p$ , and  $\alpha + \alpha + p + p$  cluster density distribution of  $^{10}\text{C}$ .

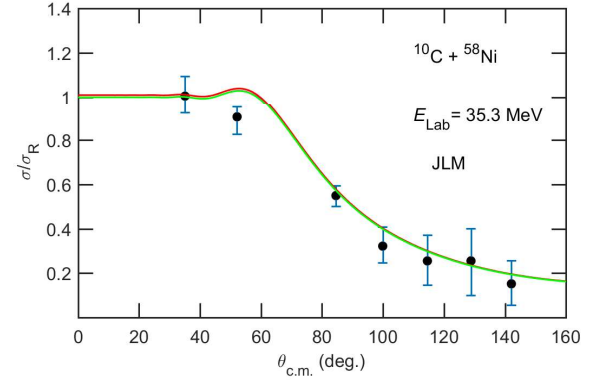
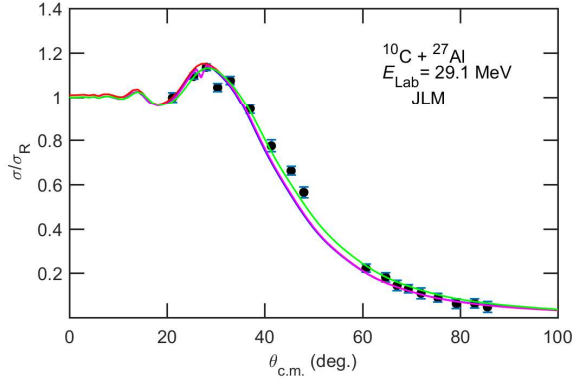
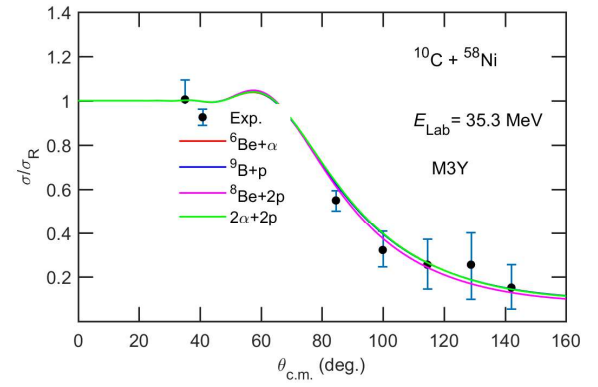
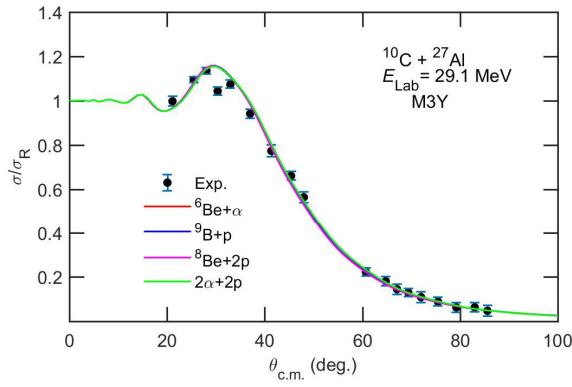


Figure 2: Elastic scattering angular distributions for  $^{10}\text{C} + ^{27}\text{Al}$  at incident energy of 29.1 MeV obtained using M3Y and JLM effective interactions with  $^6\text{Be} + \alpha$ ,  $^9\text{B} + p$ ,  $^8\text{Be} + p + p$ , and  $\alpha + \alpha + p + p$  cluster density distribution of the  $^{10}\text{C}$ . The experimental data are taken from Ref. [10].

Figure 3: Same as Figure 2 but for  $^{10}\text{C} + ^{58}\text{Ni}$  at incident energy of 35.3 MeV. The experimental data are taken from Ref. [12].

## 2.2. Effective nucleon-nucleon interaction

The two different forms of effective NN interactions considered in the present study are fully described elsewhere [18, 19, 20]. As such, only salient details are provided here.

### 2.2.1. M3Y interaction

The density-independent M3Y interaction is derived by Bertsch *et al.*, [19] and parameterized according to Satchler and Love [20] as follows:

$$v_{\text{NN}}^{\text{M3Y}}(r) = 7999 \frac{\exp(-4r)}{4r} - 2134 \frac{\exp(-2.5r)}{2.5r} - 276 \left[ 1 - 0.005 \frac{E_{\text{Lab}}}{A_{\text{P}}} \right] \delta(r), \quad (7)$$

where  $E_{\text{Lab}}$  and  $A_{\text{P}}$  are the laboratory energy and mass number of the projectile, respectively. The first and the second terms represent the direct part while the third term represents the exchange part of the interaction potential.

### 2.2.2. JLM interaction

The JLM potential derived by Jeukenne, Lejeune and Mahaux [18] was obtained in a Brueckner-Hartree-Fock (BHF) approximation from the Reid soft-core NN interaction. The

isoscalar component of the complex JLM interaction has the form [18]:

$$v_{\text{NN}}^{\text{JLM}}(s, \rho, E) = g(s)v_0(\rho, E) + ig(s)w_0(\rho, E), \quad (8)$$

where  $g(s)$ ,  $v_0$  and  $w_0$  are the radial dependence factor, the real component and the imaginary component of the effective interaction, respectively. In this study, only the real part of the JLM effective interaction is considered and discussed, the imaginary part is replaced with the Woods-Saxon potential (Eq. 6). The density and energy dependence of the real part of JLM interaction is parametrized as follows [18]:

$$v_0 = \sum_{i,j=1}^3 a_{ij} \rho^{i-1} E^{j-1}. \quad (9)$$

The values of the coefficient  $a_{ij}$  are taken from Ref. [18]. In this study, the local-density approximation (LDA) is considered using the arithmetic average approach as prescribed in Ref. [21]:

$$\rho = (\rho_p(r_1)\rho_T(r_2))^{1/2}, \quad (10)$$

where the local density is evaluated at each position of the interacting nucleons. The radial dependence factor is taken to be a single-Gaussian shape [22]

$$g(s) = (t\sqrt{\pi})^{-3} \exp(-s^2/t^2) \quad (11)$$

with  $t = 1.2$  fm.

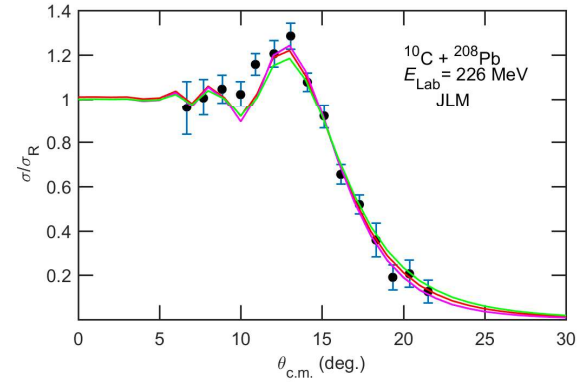
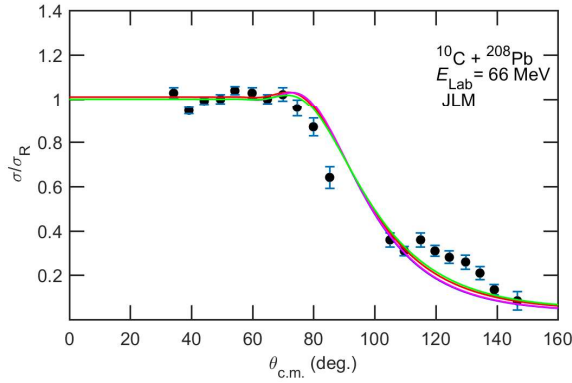
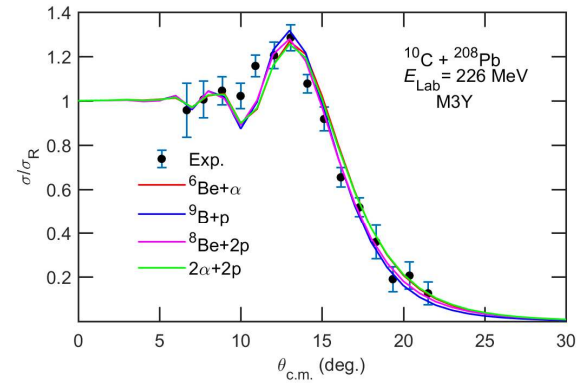
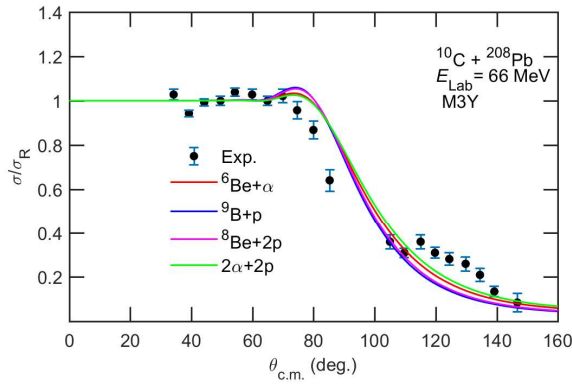


Figure 4: Same as Figure 2 but for  $^{10}\text{C} + ^{208}\text{Pb}$  at incident energy of 66 MeV. The experimental data are taken from Ref. [8].

Figure 5: Same as Figure 2 but for  $^{10}\text{C} + ^{208}\text{Pb}$  at  $E_{\text{Lab}} = 226$  MeV. The experimental data are taken from Ref. [7].

### 2.3. Cluster density distribution of $^{10}\text{C}$ nucleus

The present work considers a simple cluster model, which simply involves adding together the densities of the constituent cluster nuclei. As an example, the density for  $^{10}\text{C}$ , is expressed as,  $\rho^{10\text{C}} = \rho^{6\text{Be}} + \rho_{\alpha}$ , implying that the clusters are overlapping at the same point inside the nucleus. Such an oversimplified approach may still have some merit since in a more realistic calculation, one would have to consider an overlap of the cluster nuclei using the appropriate Jacobi coordinates, which, for the case of three or four clusters can turn out to be very complicated for the present investigation. The cluster model density distribution has been used successfully to analyze elastic scattering cross sections of unstable projectile nuclei (see, e.g., Refs. [23, 24, 25, 26, 27, 28]). Four different forms of cluster density distributions of the projectile nucleus are considered in this study and each is presented in the following section.

#### 2.3.1. $^6\text{Be} + \alpha$ system

Firstly, the  $^{10}\text{C}$  nucleus is taken to be a cluster of  $^6\text{Be}$  and  $\alpha$  nuclei. Hence, the density distribution of  $^{10}\text{C}$  takes the form:

$$\rho^{10\text{C}} = \rho^{6\text{Be}} + \rho_{\alpha}. \quad (12)$$

The São Paulo (SP) density distribution [29], is used for the density of  $^6\text{Be}$  and parametrized as follows:

$$\rho_{i^6\text{Be}}(r) = \rho_{0i} \left( 1 + \exp\left(\frac{r - R_i}{a_i}\right) \right)^{-1}, \quad (i = n, p), \quad (13)$$

where

$$R_n = 1.49N^{1/3} - 0.79, \quad R_p = 1.81Z^{1/3} - 1.12, \quad (14)$$

and

$$a_n = 0.47 + 0.00046N, \quad a_p = 0.47 - 0.00083Z. \quad (15)$$

Here,  $R_n(R_p)$  and  $a_n(a_p)$  represent the half-density radius and surface thickness parameter of neutron (proton), while  $Z$  and  $N$  are proton and neutron numbers, respectively. The  $\alpha$  density is taken to be [20]

$$\rho_{\alpha} = 0.4229 \exp(-0.7024r^2). \quad (16)$$

#### 2.3.2. $^9\text{B} + p$ system

Another cluster density of  $^{10}\text{C}$  considered in this study is given by

$$\rho^{10\text{C}} = \rho^9\text{B} + \rho_p, \quad (17)$$

where the density distribution of  $^9\text{B}$  is given in Eq. 13, and that of proton is taken to be [30, 31]

$$\rho_p = (\beta\pi)^{-3} \exp(-r^2/\beta^2), \quad (18)$$

where  $\beta$  is adjusted to reproduce the rms radius value of  $^{10}\text{C}$ .

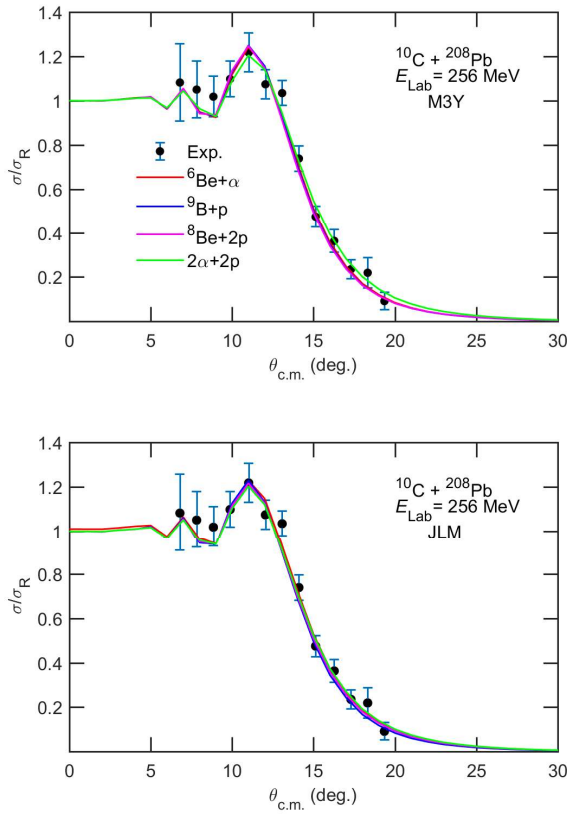


Figure 6: Same as Figure 2 but for  $^{10}\text{C} + ^{208}\text{Pb}$  at incident energy of 256 MeV. The experimental data are taken from Ref. [7].

### 2.3.3. $^8\text{Be} + p + p$ system

The density distribution of  $^{10}\text{C}$  can also be evaluated as the sum of  $^8\text{Be}$ ,  $p$  and  $p$  densities

$$\rho^{10\text{C}} = \rho^{8\text{Be}} + \rho_p + \rho_p, \quad (19)$$

where the density distributions of  $^8\text{Be}$  and  $p$  are given in Eqs. 13 and 18, respectively.

### 2.3.4. $\alpha + \alpha + p + p$ system

The last density distribution form of  $^{10}\text{C}$  considered here is obtained from the addition of density distributions of  $\alpha$ ,  $\alpha$ ,  $p$  and  $p$

$$\rho^{10\text{C}} = \rho_\alpha + \rho_\alpha + \rho_p + \rho_p, \quad (20)$$

where the density distributions of  $\alpha$  and  $p$  are given Eqs. 16 and 18, respectively. The approach of obtaining nuclear density as a sum of the densities of the clusters has been used in Refs. [23, 24].

## 3. Method of calculation

The first step in calculating elastic scattering cross section is to obtain the complex total optical potential. In the present study, the real part of the total optical potentials is calculated via the double folding approach as expressed in Eq. 4 using

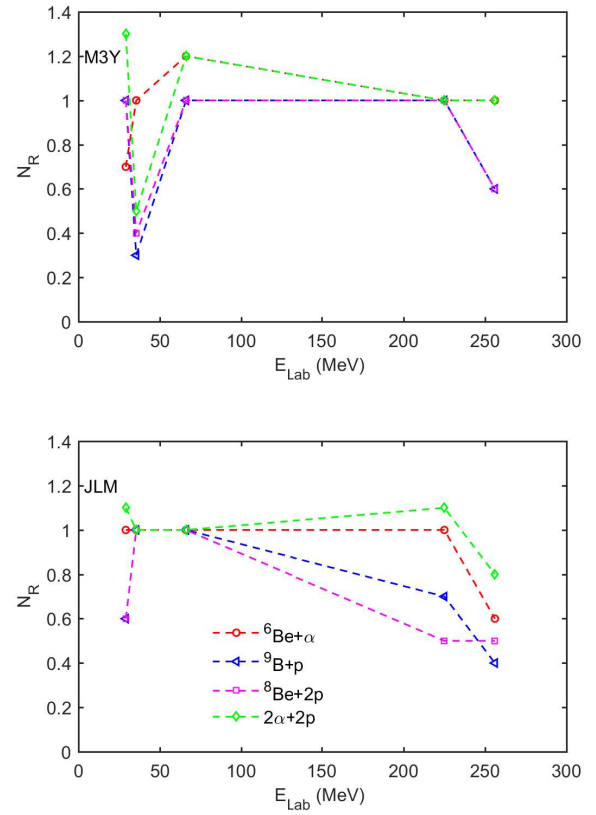


Figure 7: Normalization constant,  $N_R$  versus incident energy,  $E_{\text{Lab}}$  obtained for  $^{10}\text{C} + ^{27}\text{Al}$  at 29.1 MeV,  $^{10}\text{C} + ^{58}\text{Ni}$  at 35.3 MeV and  $^{10}\text{C} + ^{208}\text{Pb}$  at 66, 226 and 256 MeV, using M3Y and JLM effective interactions with  $^6\text{Be} + \alpha$ ,  $^9\text{B} + p$ ,  $^8\text{Be} + p + p$ , and  $\alpha + \alpha + p + p$  cluster density distribution of  $^{10}\text{C}$ . The dashed curves are to guide the eye.

M3Y and JLM effective  $NN$  interactions with  $^6\text{Be} + \alpha$ ,  $^9\text{B} + p$ ,  $^8\text{Be} + p + p$ , and  $\alpha + \alpha + p + p$  cluster density distribution of the  $^{10}\text{C}$ . The folded potentials are obtained using the computer code DF POT [32].

The elastic scattering cross sections of  $^{10}\text{C}$  are evaluated with the computer code PTOLEMY [33, 34]. The code takes as input the obtained folded potential to represent the real part of the optical potential while the imaginary part of the potential is taken in the usual phenomenological form as expressed in Eq. 6. These potential are used to analyze experimental data of  $^{10}\text{C} + ^{27}\text{Al}$  (at 29.1 MeV) [10],  $^{10}\text{C} + ^{58}\text{Ni}$  (at 35.3 MeV) [12] and  $^{10}\text{C} + ^{208}\text{Pb}$  (at 66, 226 and 256 MeV) [7, 8]. In order to reduce the number of fitting parameters, the imaginary reduced radius,  $r_I$  and diffuseness parameter  $a_I$  are fixed at 1.3 and 0.4 fm, respectively.

Finally, in order to assess the quality of agreement between the calculated results and experimental data, a search on  $N_R$  and  $W_1$  was carried out using the usual reduced chi-square approach [20]

$$\chi^2 = N^{-1} \sum_{k=1}^N \left[ \frac{\sigma_{\text{cal}}(\theta_k) - \sigma_{\text{ex}}(\theta_k)}{\Delta\sigma_{\text{ex}}(\theta_k)} \right]^2, \quad (21)$$

where  $\sigma_{\text{cal}}(\theta_k)$  and  $\sigma_{\text{ex}}(\theta_k)$  are the calculated and experimental cross sections, respectively,  $\Delta\sigma_{\text{ex}}(\theta_k)$  is the experimental error,

Table 2: Real normalization parameter, depth of the imaginary potential ( $W_I$ ), real and imaginary volume integrals ( $J_R$  and  $J_I$ ), total reaction cross sections ( $\sigma_R$ ) and  $\chi^2/N$  values for the elastic  $^{10}\text{C}$  scattering on  $^{27}\text{Al}$ ,  $^{58}\text{Ni}$ , and  $^{208}\text{Pb}$  target nuclei. The imaginary radius  $r_I$  and diffuseness  $a_I$  are fixed at 1.3 and 0.4 fm, respectively.

System	$E_{\text{Lab}}$ (MeV)	Potential	Cluster	$N_R$	$W_I$ (MeV)	$J_R$ (MeVfm <sup>3</sup> )	$J_I$ (MeVfm <sup>3</sup> )	$\sigma_R$ (mb)	$\chi^2/N$			
$^{10}\text{C}+^{27}\text{Al}$	29.1	M3Y	$^6\text{Be}+\alpha$	1.0	10.5	416.610	50.729	779.86	0.42			
			$^9\text{B}+p$	1.0	33.5	416.365	161.856	904.88	0.94			
			$^8\text{Be}+p+p$	1.0	30.5	416.783	147.355	894.90	0.91			
			$\alpha+\alpha+p+p$	1.3	10.5	416.610	50.729	775.29	0.37			
		JLM	$^6\text{Be}+\alpha$	1.0	55.5	345.483	268.139	967.45	0.56			
			$^9\text{B}+p$	0.6	55.5	536.506	268.139	910.88	0.61			
			$^8\text{Be}+p+p$	0.6	50.5	524.859	243.982	951.23	0.68			
			$\alpha+\alpha+p+p$	1.1	40.5	182.643	195.669	910.88	0.41			
			$^{10}\text{C}+^{58}\text{Ni}$	35.3	M3Y	$^6\text{Be}+\alpha$	0.7	52.5	415.575	186.713	469.23	2.33
						$^9\text{B}+p$	0.3	52.5	415.017	186.713	469.61	2.23
$^8\text{Be}+p+p$	0.4	50.5				415.146	179.600	476.74	2.75			
$\alpha+\alpha+p+p$	0.5	50.5				415.559	179.600	465.91	2.35			
JLM	$^6\text{Be}+\alpha$	1.0			40.0	325.934	142.257	535.16	2.39			
	$^9\text{B}+p$	1.0			40.0	500.371	142.257	535.15	2.42			
	$^8\text{Be}+p+p$	1.0			40.0	489.754	142.257	535.16	2.44			
	$\alpha+\alpha+p+p$	1.0			40.0	176.553	142.257	535.16	2.42			
	$^{10}\text{C}+^{208}\text{Pb}$	66.0			M3Y	$^6\text{Be}+\alpha$	1.2	300.5	406.2207	595.5052	662.66	16.87
						$^9\text{B}+p$	1.0	250.5	402.3044	496.4195	672.49	20.50
$^8\text{Be}+p+p$			1.0	250.5		402.7722	496.4195	664.92	19.79			
$\alpha+\alpha+p+p$			1.2	300.5		407.7502	595.5052	648.46	15.80			
JLM			$^6\text{Be}+\alpha$	1.0	450.5	353.997	892.76	708.24	15.56			
			$^9\text{B}+p$	1.0	380.5	428.733	754.042	701.56	16.78			
			$^8\text{Be}+p+p$	1.0	380.5	424.329	754.042	699.67	16.88			
			$\alpha+\alpha+p+p$	1.0	450.5	287.292	892.763	699.28	15.61			
			$^{10}\text{C}+^{208}\text{Pb}$	226.0	M3Y	$^6\text{Be}+\alpha$	1.0	30.0	384.199	59.451	3054.40	3.60
						$^9\text{B}+p$	1.0	30.5	380.620	60.422	3087.70	1.94
$^8\text{Be}+p+p$	1.0	25.5				380.867	50.534	3046.90	2.39			
$\alpha+\alpha+p+p$	1.0	40.5				385.806	80.26	3108.2	5.48			
JLM	$^6\text{Be}+\alpha$	1.0			50.5	666.353	100.0765	3182.6	1.65			
	$^9\text{B}+p$	0.7			40.5	211.937	80.259	3138.7	1.66			
	$^8\text{Be}+p+p$	0.5			40.5	445.607	80.259	3138.1	1.98			
	$\alpha+\alpha+p+p$	1.1			50.5	1040.987	100.0766	3168.8	2.11			
	$^{10}\text{C}+^{208}\text{Pb}$	256.0			M3Y	$^6\text{Be}+\alpha$	1.0	30.0	384.203	59.451	3164.4	1.46
						$^9\text{B}+p$	0.6	30.0	381.022	59.451	3163.7	1.33
$^8\text{Be}+p+p$			0.6	32.5		381.016	64.406	3184.6	1.36			
$\alpha+\alpha+p+p$			1.0	30.5		386.112	60.442	3154.1	3.47			
JLM			$^6\text{Be}+\alpha$	0.6	40.5	1103.551	80.259	3240.2	1.06			
			$^9\text{B}+p$	0.4	40.5	401.396	80.259	3245.1	1.25			
			$^8\text{Be}+p+p$	0.5	40.5	240.516	80.259	3238.0	1.22			
			$\alpha+\alpha+p+p$	0.8	40.5	1681.423	80.259	3234.5	1.65			

and  $N$  is the number of data points. An average value of 10% error is used as uncertainty on all the experimental data used in this study.

The real ( $J_R$ ) and imaginary ( $J_I$ ) volume integrals are com-

puted using the expressions

$$J_R(E) = \frac{4\pi}{A_P A_T} \int V(r, E) r^2 dr, \quad (22)$$

Table 3: Reduced reaction cross sections,  $\sigma_{\text{Re}}^{\text{M3Y}}$  and  $\sigma_{\text{Re}}^{\text{JLM}}$ , obtained in this work using M3Y and JLM potentials, respectively, compared with  $\sigma_{\text{Re}}^{\text{SPP}}$  obtained from SPP in Refs.[7, 8, 10].

System	$E_{\text{Lab}}$ (MeV)	$E_{\text{Re}}$ (MeV)	Cluster	$\sigma_{\text{Re}}^{\text{M3Y}}$ (mb)	$\sigma_{\text{Re}}^{\text{JLM}}$ (mb)	$\sigma_{\text{Re}}^{\text{SPP}}$ (mb)
$^{10}\text{C} + ^{27}\text{Al}$	29.1	1.402	$^6\text{Be} + \alpha$	29.353	36.414	36.736 [10]
			$^9\text{B} + p$	34.058	34.285	
			$^8\text{Be} + p + p$	33.683	35.803	
			$\alpha + \alpha + p + p$	29.181	34.285	
$^{10}\text{C} + ^{58}\text{Ni}$	35.3	1.079	$^6\text{Be} + \alpha$	12.925	14.741	
			$^9\text{B} + p$	12.935	14.741	
			$^8\text{Be} + p + p$	13.132	14.741	
			$\alpha + \alpha + p + p$	12.833	14.741	
$^{10}\text{C} + ^{208}\text{Pb}$	66.0	1.034	$^6\text{Be} + \alpha$	10.151	10.850	14.474 [8]
			$^9\text{B} + p$	10.302	10.747	
			$^8\text{Be} + p + p$	10.186	10.718	
			$\alpha + \alpha + p + p$	9.934	10.712	
	226.0	3.541	$^6\text{Be} + \alpha$	46.791	48.755	48.685 [7]
			$^9\text{B} + p$	47.301	48.083	
			$^8\text{Be} + p + p$	46.676	48.073	
			$\alpha + \alpha + p + p$	47.615	48.544	
	256.0	4.011	$^6\text{Be} + \alpha$	48.476	49.638	50.079 [7]
			$^9\text{B} + p$	48.466	49.713	
			$^8\text{Be} + p + p$	48.786	49.604	
			$\alpha + \alpha + p + p$	48.319	49.550	

and

$$J_1(E) = \frac{4\pi}{A_{\text{P}}A_{\text{T}}} \int W(r, E)r^2 dr, \quad (23)$$

respectively.

#### 4. Result and discussion

The real part of the optical potentials is calculated for the reactions  $^{10}\text{C} + ^{27}\text{Al}$  at 29.1 MeV,  $^{10}\text{C} + ^{58}\text{Ni}$  at 35.3 MeV, and  $^{10}\text{C} + ^{208}\text{Pb}$  at 66, 226 and 256 MeV using the double folding model (Eq. 4) with M3Y and JLM effective  $NN$  interactions, and four  $^{10}\text{C}$  cluster structure densities viz.  $^6\text{Be} + \alpha$ ,  $^9\text{B} + p$ ,  $^8\text{Be} + p + p$ , and  $\alpha + \alpha + p + p$ . Typical calculated folding potentials (with  $N_{\text{R}} = 1$ ) for the reactions  $^{10}\text{C} + ^{27}\text{Al}$  at 29.1 MeV,  $^{10}\text{C} + ^{58}\text{Ni}$  at 35.3 MeV and  $^{10}\text{C} + ^{208}\text{Pb}$  at 66 MeV are shown in Figure 1. It can be seen that the M3Y potentials obtained differ primarily in depth and shape from the JLM potentials. Furthermore, for the M3Y potential, the folding potentials computed using the  $\alpha + \alpha + p + p$  configuration are observed to be deeper than those obtained from the three other  $^{10}\text{C}$  cluster density distributions. On the other hand, the use of the  $^9\text{B} + p$  cluster density results in potentials with a shallower depth compared to the other cluster configurations. In contrast, for the JLM potential, the  $^9\text{B} + p$  cluster configuration produces a deeper potential compared to the other cluster configurations.

The elastic scattering cross sections of the reactions under investigation are calculated using folded real potential and Woods-Saxon imaginary potential with the four different forms of cluster densities for  $^{10}\text{C}$ . The results of the calculations are compared with appropriate experimental data and are shown in Figures 2 - 6. The parameters that give good agreement with experimental data, the real volume integral,  $J_{\text{R}}$ , imaginary volume integral,  $J_1$  and the reaction cross sections,  $\sigma_{\text{R}}$  for all the reactions considered are presented in Table 2. It can be seen from the figures, and values of  $N_{\text{R}}$  and  $\chi^2/N$  in Table 2 that the cross section obtained using M3Y and JLM interactions give almost the same quality of fit to experimental data. However, the values of  $\sigma_{\text{R}}$  obtained for the JLM interaction are higher than that of M3Y.

The elastic scattering cross sections of  $^{10}\text{C} + ^{27}\text{Al}$  at incident energy 29.1 MeV are investigated for  $^6\text{Be} + \alpha$ ,  $^9\text{B} + p$ ,  $^8\text{Be} + p + p$ , and  $\alpha + \alpha + p + p$  cluster densities of  $^{10}\text{Ca}$ , and the results are shown in Figure 2. The results obtained using M3Y  $NN$  interactions are shown in the top panel while the bottom panel displays the results obtained with JLM interaction. An excellent agreement between calculated results and data is observed. Also, the results show similar shape for the different cluster configurations.

Figure 3 shows the elastic scattering cross sections of  $^{10}\text{C} + ^{58}\text{Ni}$  at 35.3 MeV obtained using the aforementioned set of cluster densities for  $^{10}\text{C}$  and the two effective interactions M3Y and JLM. Again, the theoretical results agree reasonably well

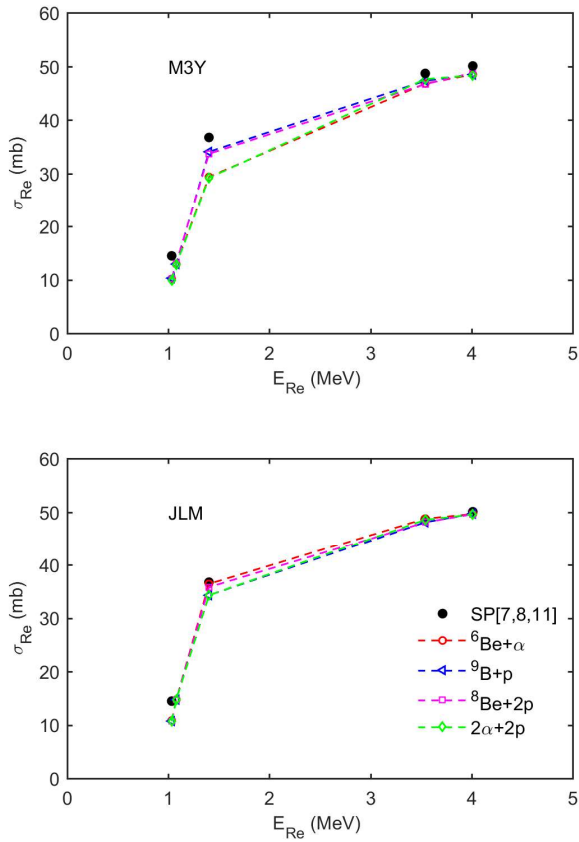


Figure 8: Reduced reaction cross sections,  $\sigma_{Re}$ , from the present work and other results from Refs. [7, 8, 10] with respect to the reduced incident energy,  $E_{Re}$ . The curves are to guide the eye.

with the experimental data.

Finally, the theoretical results of elastic scattering cross sections of  $^{10}\text{C}$  from  $^{208}\text{Pb}$  at 66, 226 and 256 MeV using DF model with the four different cluster densities the two effective interactions are shown and compared with experimental data in Figures 4 - 6. Overall, good agreement is obtained between experiment and theory, except at 66 MeV where theoretical results underestimates experimental ones in the angular region  $115^\circ - 140^\circ$ . Similar discrepancy was reported for the same data in Ref. [8]. The increase of the elastic cross sections at these backward angles was attributed to coupling to excited states in the projectile nucleus and target nucleus, and this was not captured in the calculations presented in this study.

The renormalization factor  $N_R$  is usually applied to folding potential in order to assess the performance of the DF model in describing a nuclear reaction [20]. The values of  $N_R$  used for the different cluster density configurations and the different interactions considered in this study are presented in Table 2 and Figure 7. In general, it can be seen that the M3Y and JLM interactions show the need for almost the same renormalization factor  $N_R$ . Also, the values of  $N_R$  are mostly or close to unity, except for the cases of  $^9\text{B} + p$ , and  $^8\text{Be} + p + p$  in  $^{10}\text{C} + ^{58}\text{Ni}$  (with M3Y) and  $^{10}\text{C} + ^{208}\text{Pb}$  at 226 MeV (with JLM) where the potentials are heavily reduced ( $N_R = 0.3$  to  $0.5$ ). In Figure 7,

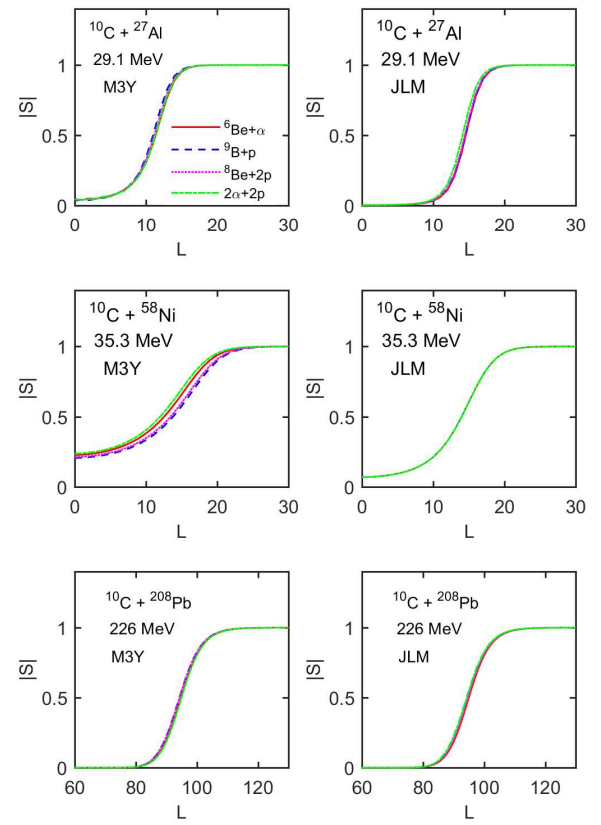


Figure 9: Modulus of the scattering matrix  $|S_L|$  versus the orbital angular momentum  $L$  obtained for  $^{10}\text{C} + ^{27}\text{Al}$  at 29.1 MeV,  $^{10}\text{C} + ^{58}\text{Ni}$  at 35.3 MeV and  $^{10}\text{C} + ^{208}\text{Pb}$  at 226 MeV, using M3Y and JLM effective interactions with  $^6\text{Be} + \alpha$ ,  $^9\text{B} + p$ ,  $^8\text{Be} + p + p$ , and  $\alpha + \alpha + p + p$  cluster density distribution of the  $^{10}\text{C}$ .

the  $N_R$  values obtained for both the M3Y and JLM interactions are plotted versus the incident energy  $E_{Lab}$ . One observes from this plot that for both interactions the  $^6\text{Be} + \alpha$  cluster density generally give  $N_R$  value closer to unity than other cluster configurations. Also, from this figure, one sees that in the case of  $^{10}\text{C} + ^{58}\text{Ni}$  reaction using M3Y potential, the potential is strongly reduced almost for all the cluster configurations. This might be due to the presence of other reaction mechanisms not considered in our calculations, such as the inclusion of the  $2^+$  excited state of the  $^{10}\text{C}$  nucleus, as mentioned in Ref. [12].

The real volume integrals  $J_R$  values obtained for both the M3Y and JLM interactions as well as the corresponding reaction cross sections  $\sigma_R$  for each cluster configuration are presented in Table 2. One can see that the difference in the value of the reaction cross section for the various cluster configurations considered under the same potential is not more than 3%, except for the reaction  $^{10}\text{C} + ^{27}\text{Al}$  under the M3Y potential where the difference is as high as 13%. In general, the cluster configuration  $^9\text{B} + p$  gives slightly higher value of  $\sigma_R$  compared to the other three cluster configurations. Furthermore, in order to compare the reaction cross sections of the different potentials and densities with each other and with data from literature, a reduction method is used. The reduced reaction cross section

and reduced energy are given as follows [35]

$$\sigma_{\text{Re}} = \frac{\sigma_{\text{R}}}{(A_{\text{P}}^{1/3} + A_{\text{T}}^{1/3})^2}, \quad (24)$$

and

$$E_{\text{Re}} = E_{\text{c.m.}} \times \frac{A_{\text{P}}^{1/3} + A_{\text{T}}^{1/3}}{Z_{\text{P}}Z_{\text{T}}}, \quad (25)$$

where  $E_{\text{c.m.}}$  is the incident energy in the center of mass frame, and  $Z_{\text{P(T)}}$  is the proton number of the projectile (target) nucleus. The reduced energy and reaction cross section values for the different potentials are listed in Table 3 and shown in Figure 8. The black filled circle represents the results obtained by Yang *et al.*, [7], Linares *et al.*, [8] and Aguilera *et al.*, [10], using SPP potential. It can be seen from the lower panel of Figure 8 that the results obtained with JLM potential agree reasonably well with that of SPP potential for all the reactions, with the exception of  $^{10}\text{C} + ^{208}\text{Pb}$  at 66 MeV where the SPP gives higher reaction cross section (see Table 3). In the upper panel of the figure, it can be seen that the  $\sigma_{\text{Re}}$  obtained for M3Y potentials are consistently lower than that reported for SPP. In general, as shown in Table 3 and Figure 8, one observes that for the M3Y effective interaction the cluster configuration  $^9\text{B} + p$  gives slightly higher value of  $\sigma_{\text{Re}}$  compared to the other three cluster configurations. For the case of JLM interaction, the cluster configuration  $^6\text{Be} + \alpha$  gives slightly higher value of  $\sigma_{\text{Re}}$  compared to the other three cluster configurations.

The last parameter presented in Table 2 is the reduced chi-square value  $\chi^2/N$ . It can be seen that, in general, the  $\chi^2/N$  values are small, which is an indication of good agreement between the calculated and experimental cross sections.

Figure 9 shows the plot of the magnitudes of partial-wave scattering (S-matrix) elements  $|S_L|$  versus the orbital angular momentum  $L$ , calculated for reactions  $^{10}\text{C} + ^{27}\text{Al}$  at 29.1 MeV,  $^{10}\text{C} + ^{58}\text{Ni}$  at 35.3 MeV and  $^{10}\text{C} + ^{208}\text{Pb}$  at 226 MeV, using the M3Y and JLM potentials. In this figure, we see that the value of  $|S_L| \approx 0$  at small  $L$  and increases rapidly as  $L$  becomes larger, and finally reaches unity. The value of  $|S_L|$  indicates the level of absorption. For example, it is known that  $|S_L| = 1$  for elastic scattering means no absorption. Furthermore, it has been suggested that total absorption happens when the transmission coefficient  $(1 - |S_L|^2)$  equals zero [36]. It can be seen from Figure 9 that the values of  $L$  obtained for both M3Y and JLM potentials, increase with increasing target mass number. Furthermore, the range of the values of  $L$  required for  $|S_L|$  to rise from 0 to 1 is slightly higher for JLM than for M3Y potential. Lastly, it is observed that  $|S_L|$  does not show significant sensitivity to the project cluster densities under the same potentials.

## 5. Conclusions

A systematic analysis of elastic scattering cross sections of  $^{10}\text{C} + ^{27}\text{Al}$ ,  $^{10}\text{C} + ^{58}\text{Ni}$ , and  $^{10}\text{C} + ^{208}\text{Pb}$  reactions has been performed within the framework of the double-folding optical model. This is with the view to investigating the nuclear structure of the  $^{10}\text{C}$  nuclei via the simple cluster model as well as

study the sensitivity of  $^{10}\text{C}$  elastic scattering cross sections to different effective  $NN$  interactions. The real part of the optical potential is constructed by folding two different effective  $NN$  interactions M3Y and JLM, with the density  $^{10}\text{C}$ . A cluster model density distribution is assumed for  $^{10}\text{C}$  and four different cluster configurations are considered, namely,  $^6\text{Be} + \alpha$ ,  $^9\text{B} + p$ ,  $^8\text{Be} + p + p$ , and  $\alpha + \alpha + p + p$ . A phenomenological WS form is used for imaginary part. For the reactions considered in this study, the values of the reduced radius  $r_1$ , and the diffuseness parameter  $a_1$  of the WS potential are fixed at 1.3 and 0.4 fm, respectively, while the depth  $W_0$  is adjusted to fit the data.

A comparative study of the four cluster configurations for  $^{10}\text{C}$  shows that the results obtained with  $^6\text{Be} + \alpha$ ,  $^9\text{B} + p$ ,  $^8\text{Be} + p + p$  and  $\alpha + \alpha + p + p$  cluster configurations describe the experimental data quantitatively well. However, in terms of  $N_R$ ,  $\sigma_R$  and  $\chi^2/N$ , the  $^6\text{Be} + \alpha$  and  $^9\text{B} + p$  cluster configurations yield better description of the experimental data than the other cluster configurations. Also, it is clear that any cluster density distribution for  $^{10}\text{C}$  can be compensated by the parameters  $W_0$  and  $N_R$ . This further confirms the cluster structure of  $^{10}\text{C}$  nucleus.

In addition, a study of the effect of effective  $NN$  interactions on the elastic scattering cross sections of the reactions considered in this study reveals that the JLM interactions is as good as the popular M3Y interactions in terms of their agreements with experimental data. However, the JLM potential gives higher  $\sigma_R$  value than the M3Y potentials. The theoretical calculations from both M3Y and JLM effective interactions with cluster density distributions of  $^{10}\text{C}$  ( $^6\text{Be} + \alpha$ ,  $^9\text{B} + p$ ,  $^8\text{Be} + p + p$ , and  $\alpha + \alpha + p + p$ ) provide good description of the experimental data for all the reactions considered in this work.

Furthermore, this study highlights the importance of considering the overlap of cluster nuclei using appropriate Jacobi coordinates in a more realistic calculation. Future research can focus on developing more sophisticated models to account for the complex structure and dynamics of three or four-cluster nuclei and their overlap.

Overall, this study provides valuable insights into the reaction dynamics of complex nuclear systems and can potentially inform the design and development of future nuclear reactors and other applications that require a detailed understanding of nuclear reactions.

## References

- [1] L. Canto, P. Gomes, R. Donangelo, J. Lubian, and M. S. Hussein, "Recent developments in fusion and direct reactions with weakly bound nuclei", *Phys. Rep.* **596** (2015) 1. <https://doi.org/10.1016/j.physrep.2015.08.001>
- [2] N. Keeley, R. Raabe, N. Alamanos, and J. Sida, "Fusion and direct reactions of halo nuclei at energies around the Coulomb barrier", *Prog. in Part. and Nucl. Phys.* **59**, (2007) 579. <https://doi.org/10.1016/j.pnpnp.2007.02.002>
- [3] D. Savran, T. Aumann, and A. Zilges, "Experimental studies of the Pygmy Dipole Resonance", *Prog. in Part. and Nucl. Phys.* **70** (2013) 210. <http://dx.doi.org/10.1016/j.pnpnp.2013.02.003>
- [4] L. F. Canto, V. Guimarães, J. Lubián, and M. S. Hussein, "The total reaction cross section of heavy-ion reactions induced by stable and unstable exotic beams: the low-energy regime", *Eur. Phys. J. A* **56** (2020) 281. <https://doi.org/10.1140/epja/s10050-020-00277-8>

- [5] J. Wang et al., “ $^7\text{Be}$ ,  $^8\text{B}+^{208}\text{Pb}$  Elastic scattering at above-barrier energies”, *J. of Phys.: Conf. Series* **420** (2013) 012075. <https://doi.org/10.1088/1742-6596/420/1/012075>
- [6] T. Aumann and C. A. Bertulani, “Indirect methods in nuclear astrophysics with relativistic radioactive beams”, *Prog. in Part. and Nucl. Phys.* **112** (2020) 103753. <https://doi.org/10.1016/j.pnpnp.2019.103753>
- [7] Y. Y. Yang et al., “Quasi-elastic scattering of  $^{10,11}\text{C}$  and  $^{10}\text{B}$  from a  $^{208}\text{Pb}$  target”, *Phys. Rev. C* **90** (2014) 014606. <https://doi.org/10.1103/PhysRevC.90.014606>
- [8] R. Linares et al., “Elastic scattering measurements for the  $^{10}\text{C}+^{208}\text{Pb}$  system at  $E_{\text{Lab}} = 66$  MeV”, *Phys. Rev. C* **103** (2021) 044613. <https://doi.org/10.1103/PhysRevC.103.044613>
- [9] N. Curtis et al., “Breakup reaction study of the Brunian nucleus  $^{10}\text{C}$ ”, *Phys. Rev. C* **77** (2008) 021301(R). <http://dx.doi.org/10.1103/PhysRevC.77.021301>
- [10] E. F. Aguilera et al., “Elastic scattering of  $^{10}\text{C}+^{27}\text{Al}$ ”, *IOP Conf. Series: J. of Phys.: Conf. Series* **876** (2017) 012001. <http://dx.doi.org/10.1088/1742-6596/876/1/012001>
- [11] M. Aygun, “Analysis with relativistic mean-field density distribution of elastic scattering cross-sections of carbon isotopes ( $^{10-14,16}\text{C}$ ) by various target nuclei”, *Pramana - J. Phys.* **93** (2019) 72. <https://doi.org/10.1007/s12043-019-1835-y>
- [12] V. Guimarães et al., “Strong coupling effect in the elastic scattering of the  $^{10}\text{C}+^{58}\text{Ni}$  system near barrier”, *Phys. Rev. C* **100** (2019) 034603. <https://doi.org/10.1103/PhysRevC.100.034603>
- [13] M. Aygun, “Comprehensive Research of  $^{10}\text{C}$  nucleus using different theoretical approaches”, *Ukr. J. Phys.* **66** (2021) 8. <https://doi.org/10.15407/ujpe66.8.653>
- [14] S. D. Olorunfunmi and A. Bahini, “Microscopic analysis of elastic scattering angular distributions for five different density distribution of  $^9\text{Be}$  Nucleus”, *Phys. Atom. Nuclei* **84** (2021) 448. <https://doi.org/10.1134/S106377882104024>
- [15] M. Anwar, B. El-Naggar, and K. O. Behairy, “Microscopic analysis of the  $^8\text{B} + ^{58}\text{Ni}$  elastic scattering at energies from 20.7 to 29.3 MeV”, *J. Phys. Soc. Jpn.* **91** (2022) 014201. <https://doi.org/10.7566/JPSJ.91.014201>
- [16] W. A. Yahya, “Alpha decay half-lives of  $^{171-189}\text{Hg}$  isotopes using modified Gamow-like model and temperature dependent proximity potential”, *J. Nig. Soc. Phys. Sci.* **2** (2020) 250. <https://doi.org/10.46481/jnsps.2020.139>
- [17] S. Adams, E. Joseph, and G. Kamal, “Validation of Tritium Calibration Curve in CIEMAT/NIST Activity Measurement Using Non Linear Least Squared Fittings and Calculations of the Half-Life and Decay Constant of Potassium-40”, *J. Nig. Soc. Phys. Sci.* **4** (2022) 621. <https://doi.org/10.46481/jnsps.2022.621>
- [18] J. P. Jeukenne, A. Lejeune, and C. Mahaux, “Optical-model potential in finite nuclei from Reid’s hard core interaction”, *Phys. Rev. C* **16** (1977) 80. <https://doi.org/10.1103/PhysRevC.16.80>
- [19] G. F. Bertsch, J. Borysowicz, H. McManus, and W. G. Love, “Interactions for inelastic scattering derived from realistic potentials”, *Nucl. Phys. A* **284** (1977) 399. [https://doi.org/10.1016/0375-9474\(77\)90392-X](https://doi.org/10.1016/0375-9474(77)90392-X)
- [20] G. R. Satchler and W. G. Love, “Folding model potentials from realistic interactions for heavy-ion scattering”, *Phys. Rep.* **55** (1979) 183. [https://doi.org/10.1016/0370-1573\(79\)90081-4](https://doi.org/10.1016/0370-1573(79)90081-4)
- [21] F. Carstoiu and M. Lassau, “Microscopic description of elastic scattering and reaction cross sections of  $^6\text{Li}$  and  $^{11}\text{Li}$ ”, *Nucl. Phys. A* **597**, (1996) 269. [https://doi.org/10.1016/0375-9474\(95\)00449-1](https://doi.org/10.1016/0375-9474(95)00449-1)
- [22] O. M. Knyazov and E. F. Hefter, “An analytical folding potential for deformed nuclei”, *Z. Phys. A* **301** (1981) 277. <https://doi.org/10.1007/BF01416304>
- [23] A. A. Ibraheem, M. El-Azab Farid, and A. S. Al-Hajjaji, “Analysis of  $^8\text{B}$  proton halo nucleus scattered from  $^{12}\text{C}$  and  $^{58}\text{Ni}$  at different energies”, *Brazilian J. Phys.* **48** (2018) 507. <https://doi.org/10.1007/s13538-018-0586-4>
- [24] M. Aygun and Z. Aygun, “A theoretical study on different cluster configurations of the  $^9\text{Be}$  nucleus by using a simple cluster model”, *Nucl. Sci. Tech.* **28** (2017) 86. <https://doi.org/10.1007/s41365-017-0239-2>
- [25] M. Aygun, “A comprehensive study on the internal structure and the density distribution of  $^{12}\text{Be}$ ”, *Rev. Mex. Fis.* **62** (2016) 336.
- [26] S. M. Lukyanov et al., “Some Insights into Cluster Structure of  $^9\text{Be}$  from  $^3\text{He} + ^9\text{Be}$  Reaction”, *World J. Nucl. Sci. Technol.* **5** (2015) 265. <http://dx.doi.org/10.4236/wjnst.2015.54026>
- [27] A. G. Camacho, P. R. S. Gomes, J. Lubian, and I. Padrón, “Simultaneous optical model analysis of elastic scattering, fusion, and breakup for the  $^9\text{Be} + ^{144}\text{Sm}$  system at near-barrier energies”, *Phys. Rev. C* **77** (2008) 054606. <https://doi.org/10.1103/PhysRevC.77.054606>
- [28] Y. Sert, R. Yegin, and H. Doğan, “A theoretical investigation of  $^9\text{Be} + ^{27}\text{Al}$  reaction: phenomenological and microscopic model approximation”, *Indian J. Phys.* **89** (2015) 1093. <https://doi.org/10.1007/s12648-015-0685-9>
- [29] L. C. Chamon et al., “Toward a global description of the nucleus-nucleus interaction”, *Phys. Rev. C* **66** (2002) 014610. <https://doi.org/10.1103/PhysRevC.66.014610>
- [30] A. K. Chaudhuri, “Density distribution of  $^{11}\text{Li}$  and proton elastic scattering from  $^9\text{Li}$  and  $^{11}\text{Li}$ ”, *Phys. Rev. C* **49** (1994) 1603. <https://doi.org/10.1103/PhysRevC.49.1603>
- [31] R. A. Rego, “Closed-form expressions for cross sections of exotic nuclei”, *Nucl. Phys. A* **581** (1995) 119. [https://doi.org/10.1016/0375-9474\(94\)00424-L](https://doi.org/10.1016/0375-9474(94)00424-L)
- [32] J. Cook, “DFPOT - A program for the calculation of double folded potentials”, *Commun. Comput. Phys.* **25** (1982) 125. [https://doi.org/10.1016/0010-4655\(82\)90029-7](https://doi.org/10.1016/0010-4655(82)90029-7)
- [33] M. Rhoades-Brown, M. H. Macfarlane, S. C. Pieper, “Techniques for heavy-ion coupled-channels calculations. I. Long-range Coulomb coupling”, *Phys. Rev. C* **21** (1980) 2417. <https://doi.org/10.1103/PhysRevC.21.2417>
- [34] M. H. Macfarlane, S. C. Pieper, “Ptolemy: a program for heavy-ion direct-reaction calculations”, Argonne National Laboratory Report No. ANL-76-11, (1978) (unpublished).
- [35] P. R. S. Gomes, J. Lubian, I. Padron, and R. M. Anjos, “Uncertainties in the comparison of fusion and reaction cross sections of different systems involving weakly bound nuclei”, *Phys. Rev. C* **71** (2005) 017601. <https://doi.org/10.1103/PhysRevC.71.017601>
- [36] M. C. Mermaz, “Phase shift analysis of heavy-ion elastic scattering measured at intermediate energies”, *Z. Phys. A* **321** (1985) 613. <https://doi.org/10.1007/BF01432438>